Atmos. Chem. Phys. Discuss., 14, 18277–18314, 2014
www.atmos-chem-phys-discuss.net/14/18277/2014/
doi:10.5194/acpd-14-18277-2014

Atmospheric Chemistry and Physics Discussions

Inclusion of mountain wave-induced cooling for the formation of PSCs over the Antarctic Peninsula in a chemistry–climate model

A. Orr[1], J. S. Hosking[1], L. Hoffmann[2], J. Keeble[3], S. M. Dean[4], H. K. Roscoe[1], N. L. Abraham[5,3], S. Vosper[6], and P. Braesicke[7]

[1]British Antarctic Survey, NERC, Cambridge, UK
[2]Jülich Supercomputing Centre, Forschungszentrum Jülich, Jülich, Germany
[3]University of Cambridge, Cambridge, UK
[4]National Institute of Water and Atmospheric Research, Auckland, New Zealand
[5]National Centre for Atmospheric Science, University of Cambridge, Cambridge, UK
[6]Met Office, Exeter, UK
[7]Karlsruhe Institute of Technology, Karlsruhe, Germany

Received: 31 May 2014 – Accepted: 23 June 2014 – Published: 10 July 2014

Correspondence to: A. Orr (anmcr@bas.ac.uk)

Published by Copernicus Publications on behalf of the European Geosciences Union.

Abstract

An important source of polar stratospheric clouds (PSCs), which play a crucial role in controlling polar stratospheric ozone depletion, is from the temperature fluctuations induced by mountain waves. However, this formation mechanism is usually missing in chemistry–climate models because these temperature fluctuations are neither resolved nor parameterised. Here, we investigate the representation of stratospheric mountain wave-induced temperature fluctuations by the UK Met Office Unified Model (UM) at high and low spatial resolution against Atmospheric Infrared Sounder satellite observations for three case studies over the Antarctic Peninsula. At a high horizontal resolution (4 km) the mesoscale configuration of the UM correctly simulates the magnitude, timing, and location of the measured temperature fluctuations. By comparison, at a low horizontal resolution (2.5° × 3.75°) the climate configuration fails to resolve such disturbances. However, it is demonstrated that the temperature fluctuations computed by a mountain wave parameterisation scheme inserted into the climate configuration (which computes the temperature fluctuations due to unresolved mountain waves) are in excellent agreement with the mesoscale configuration responses. The parameterisation was subsequently used to compute the local mountain wave-induced cooling phases in the chemistry–climate configuration of the UM. This increased stratospheric cooling was passed to the PSC scheme of the chemistry–climate model, and caused a 30–50 % increase in PSC surface area density over the Antarctic Peninsula compared to a 30 year control simulation.

1 Introduction

Gravity waves generated by stratified flow passing over orography (mountain waves) that propagate into the stratosphere play a crucial role in the formation of polar stratospheric clouds (PSCs). Adiabatic temperature changes resulting from mountain wave-induced vertical displacement can drive significant localised temperature fluctuations,

ACPD
14, 18277–18314, 2014

enabling stratospheric temperatures to fall below the threshold value for PSC formation in the cold phases of these waves even if the synoptic-scale temperatures are too high. Studies of individual cases show that mountain waves formed over regions including the Antarctic Peninsula, Greenland, and northern Scandinavia are a significant source of such clouds by generating localised cooling of up to ~ 15 K (e.g. Carslaw et al., 1998a; Dörnbrack et al., 1999, 2002, 2012; Noel et al., 2009).

The threshold temperatures for PSC formation at an altitude of around 20 km depend on composition (in particular water vapour and nitric acid) and are generally assumed to be 195 K for type Ia (nitric acid trihydrate particles), 191 K for type Ib (supercooled ternary solution droplets), and 188 K for type II (water ice particles) (Pawson et al., 1995; Alfred et al., 2007). Within the centre of the Antarctic stratospheric vortex in winter, the atmosphere is so cold that temperatures are regularly below these thresholds, i.e. formation of PSCs on the synoptic-scale dominates (Campbell and Sassen, 2008). Despite this, mountain waves are an important source of PSCs above e.g. the Antarctic Peninsula in the earlier and later stages of winter when synoptic-scale temperatures can be warmer than the formation thresholds (McDonald et al., 2009; Noel and Pitts, 2012). By contrast, because of stronger planetary wave forcing, the Arctic stratospheric vortex is generally considerably warmer than that of the Antarctic. Thus, the occurrence of PSC formation temperatures on the synoptic-scale is less frequent in the Arctic (Pawson et al., 1995), thereby making mountain wave-induced PSCs an important source (Dörnbrack et al., 2001; Alexander et al., 2013). Moreover, mountain waves are a significant source of PSCs on the synoptic-scale in both the Arctic and Antarctic due to their advection far downstream of the wave event that formed them (Carslaw et al., 1999; Höpfner et al., 2006; Eckermann et al., 2009; Alexander et al., 2011).

The role of PSC particles in polar ozone chemistry is generally well understood. The conversion of passive species of chlorine and bromine to active forms that destroy stratospheric ozone in sunlight takes place on the surface of PSCs (Solomon, 1999). Furthermore, the removal of nitric acid from the atmosphere by sedimentation of PSC

ACPD
14, 18277–18314, 2014

particles leads to a slower conversion of active chlorine back into its passive species (Jensen et al., 2002). The Antarctic ozone hole has profound impacts on the Southern Hemisphere circulation and surface climate during summer (e.g. Orr et al., 2008, 2012; Thompson et al., 2011). With the continued implementation of the Montreal Protocol, recovery of the Antarctic ozone hole is generally anticipated by the end of the century. However, model predictions using coupled chemistry–climate simulations give a large range of estimates of the rate and timing of this recovery (Eyring et al., 2013). The fact that the results are model dependent suggests that some mechanisms are not yet fully understood. Similarly, simulations of the ozone hole covering the past few decades obtain a wide range of results, further questioning the value of these predictions (Austin et al., 2010). Accurate predictions of the timing are critical as this recovery will reshape Southern Hemisphere climate by no-longer counteracting the effects of increasing greenhouse gases (Polvani et al., 2011).

Therefore, to produce accurate simulations of stratospheric ozone depletion, coupled chemistry–climate models must be able to represent PSC formation mechanisms and their attendant ozone-loss chemistry due to localised dynamics such as mountain waves (Cariolle et al., 1989; Carslaw et al., 1998b; Austin et al., 2010). However, current chemistry–climate models have a spatial resolution of some hundreds of kilometres (e.g. Morgenstern et al., 2010) at the equator and are therefore only able to explicitly resolve waves with long horizontal wavelengths (Reinecke and Durran, 2009), i.e. the temperature fluctuations associated with small-scale mountain waves are missing, leading to insufficient PSC formation in the models. Consistent with this is the systematic over-prediction of high-latitude spring time ozone increases in both hemispheres by models (Carslaw et al., 1998b; Eyring et al., 2006).

Mountain wave-induced stratospheric temperature fluctuations can be detected by their associated fluctuations in temperature-sensitive satellite radiance measurements from infrared scanning instruments such as the Atmospheric Infrared Sounder (AIRS) (e.g. Alexander and Barnet, 2007; Hoffmann et al., 2013). As a nadir viewing instrument, AIRS radiance measurements have a high horizontal resolution (14 km at nadir),

ACPD
14, 18277–18314, 2014

enabling waves with short horizontal scales which are unresolved by chemistry–climate models to be visible. On the other hand, AIRS radiance measurements have a limited vertical resolution, meaning waves with short (typically ≤ 10 km) vertical scales are poorly resolved. Comparison between AIRS radiance measurements and model simulated radiance measurements (calculated using the simulated temperature field of the model as input for a radiative transfer model) provides an effective and direct means of validation of the model representation of gravity wave events (Grimsdell et al., 2010).

To improve the simulation of mountain wave-induced PSCs in a chemistry–climate model, the temperature fluctuations due to unresolved (sub-grid scale) mountain waves can be parameterised (e.g. Carslaw et al., 1999; Dean et al., 2007; Wells et al., 2011). In the parameterisation scheme of Dean et al. (2007) the mountain wave-induced temperature fluctuations were used in the cloud scheme of the HadAM3 (Hadley Centre Atmospheric Model version 3) configuration of the Met Office Unified Model (UM) to realistically represent cirrus in the upper-troposphere, which was previously underrepresented over many mountain ranges. In this study, the Dean et al. (2007) scheme is used to improve the simulation of mountain wave-induced PSCs in the UK Chemistry and Aerosol (UKCA) module, which is the chemistry–climate configuration of the UM (Sect. 5). Our approach firstly requires demonstration of the ability of the parameterisation to reasonably simulate stratospheric temperature fluctuations. This is achieved by using case studies of AIRS measurements to validate high-resolution simulations (using the mesoscale configuration of the UM) of mountain wave-induced stratospheric temperature fluctuations above the Antarctic Peninsula (Sect. 3). The Antarctic Peninsula is chosen because strong westerly winds impinging on its high topographic ridge frequently generate large-amplitude stratospheric mountain waves (Plougonven et al., 2008; Hoffmann et al., 2013) with horizontal wavelengths of ~ 300 km (as well as structures on shorter horizontal scales) and long (≥ 10 km) vertical wavelengths (Wu, 2004; Alexander and Teitelbaum, 2007), i.e. resolved by AIRS. The long vertical wavelengths result from wave refraction caused when the background wind speed is unidirectional and increases with height (see e.g. Wu and Eckermann, 2008). Following this, the Dean

ACPD
14, 18277–18314, 2014

et al. (2007) scheme is inserted into the climate configuration of the UM and its temperature fluctuations are assessed by comparing with output from the high-resolution simulations (Sect. 4). We will demonstrate below that the high-resolution simulations are in excellent agreement with the AIRS observations, and can therefore be used as a "truth" with which to investigate the performance of the parameterisation scheme. The paper finishes with a summary and discussion (Sect. 6).

2 Models, mountain wave parameterisation, data, and methodology

2.1 Models

The UM is a numerical modelling system based on non-hydrostatic dynamics which can be run with varying configurations, including for this study as a mesoscale model, a climate model, and a chemistry–climate model. The climate model is based on the HadGEM3 (Hadley Centre Global Environmental Model version 3) configuration of the UM (Hewitt et al., 2011). The UKCA chemistry–climate model (Morgenstern et al., 2009) runs within the UM climate configuration. UKCA uses a simple scheme for calculating the presence of PSC particles, based on the assumption that they are in thermodynamic equilibrium with the gas phase (e.g. Feng et al., 2011). Here, both the climate and chemistry–climate configurations are atmosphere-only models based on version 7.3 of the UM, with a horizontal resolution of N48 (96×73 grid points, or $2.5^{\circ} \times 3.75^{\circ}$) and 60 vertical levels (going up to 84 km). Version 7.3 of the UM was selected for the global modelling exercise because of its current use in a recent, comprehensive model intercomparison (SPARC, 2013).

The mesoscale model is based on version 7.6 of the UM, and is similar to that described in Orr et al. (2014). It is atmosphere-only with a model domain centered over the Antarctic Peninsula, comprising 388×460 grid points with a horizontal resolution of 4 km and 85 vertical levels (going up to 85 km). Following Webster et al. (2008), it uses the option of a fully three-dimensional potential temperature advection scheme,

ACPD
14, 18277–18314, 2014

in conjunction with reduced temporal off-centering, to better represent resolved gravity waves. Orography is interpolated from a high-resolution digital elevation model of Antarctica (version 9 of the Radarsat Antarctic Mapping Project, Liu et al., 2001). The mesoscale model is nested within a coarser resolution UM global model at a horizontal resolution of N512 (1024×769 grid points, or $0.352^\circ \times 0.234^\circ$) and 70 vertical levels (going up to 80 km), i.e. output from global model forecasts (excluding sea ice state and sea surface temperature) are used as initialisation and boundary values. Initialisation values for sea ice state and sea surface temperature for the mesoscale model were obtained from high-resolution (~ 5 km scale) daily Operational Sea Surface Temperature and Sea Ice Analysis (OSTIA) data (Donlon et al., 2011). The Met Office operational analysis is used to initialise the global model. Version 7.6 of the UM was selected for the mesoscale model as it included improvements which reduced the occurrence of spurious cooling in partially resolved valleys.

2.2 Description of the mountain wave parameterisation

By assuming that waves are forced by steady flow over a two-dimensional ridge and that vertical variations of the background atmospheric state are slowly varying (compared to the wave phase), the scheme described by Dean et al. (2007) derives generalised expressions for the maximum and minimum vertical streamline displacement (resulting in cooling and warming, respectively) associated with gravity waves induced by sub-grid scale orography (SSO). These expressions are used to compute the maximum negative $\Delta T^{-}_{\mathrm{SSO}}$ and positive $\Delta T^{+}_{\mathrm{SSO}}$ temperature fluctuations associated with the displacement, which are derived using the local potential temperature gradient (Wells et al., 2011). The overall temperature fluctuation induced is subsequently calculated as $\Delta T_{\mathrm{SSO}} = \Delta T^{+}_{\mathrm{SSO}} + \Delta T^{-}_{\mathrm{SSO}}$. Waves are launched at every model grid box over land and at every model time step.

The expressions for the maximum and minimum streamline displacement depend on both the wave phase and peak vertical streamline displacement amplitude (hereafter referred to as wave amplitude), which are determined as follows. The vertical propa-

ACPD
14, 18277–18314, 2014

gation is based on linear theory for hydrostatic waves forced by steady, stably stratified flow over a two-dimensional ridge, assuming that vertical variations of the background atmospheric state are slowly varying. McFarlane (1987) showed that under these circumstances and in the absence of dissipation mechanisms that the vertical evolution of the wave amplitude is determined by the decrease in density of the atmosphere with height and by changes in the horizontal wind speed U (resolved in the direction of the wave vector) and the Brunt–Väisälä frequency N. Dissipation mechanisms such as wave-breaking and critical level absorption are introduced by preventing the amplitude from exceeding the local "saturation amplitude" for which the wave field becomes unstable ($= U/NF_{\mathrm{sat}}$, where F_{sat} is the critical Froude number for saturation). The vertical evolution of the wave phase is determined by changes in U and N, i.e. the Scorer parameter $l (\approx N/U)$.

To complete the determination of the wave phase and amplitude, their initial values at the top of the blocked layer must be decided. The initial wave phase is set equal to zero. The initial wave amplitude is set equal to the "effective" mountain height h_{eff} ($= h - h_{\mathrm{b}}$, where h is the height of the sub-grid scale mountain and h_{b} is the height of the blocked layer that occurs at low Froude number), i.e. the maximum vertical displacement of streamlines able to pass over the top of the mountain. This is strongly dependent on the direction of the low-level wind relative to the principle axis of the SSO (which preferentially aligns as ridges), and ensures that the surface amplitude is large (small) when the wind is perpendicular (parallel) to a ridge. Here, $h = n_\sigma \sigma$, where σ is the standard deviation of the SSO height from the grid-box mean and n_σ is a constant (such that $n_\sigma \sigma$ approximates the physical envelope of the peaks), and $h_{\mathrm{b}} = h - U_0/N_0 F_{\mathrm{c}}$, where F_{c} is the critical Froude number at which flow blocking is deemed to first occur, and the subscript "0" refers to the surface layer, represented by averaging U and N between the surface and h. Note that to implement the directional dependence of the surface amplitude, U_0 is resolved in the direction perpendicular to the principle axis of the sub-grid orography (i.e. the direction of the wave vector). This differs from the

ACPD
14, 18277–18314, 2014

implementation in Dean et al. (2007) which represents the directional dependence by defining the standard deviation σ of the SSO height in the surface wind direction.

The parameterisation scheme is implemented in the climate and chemistry–climate configurations of the UM. The SSO parameters used by the scheme are based on Lott and Miller (1997). In the scheme the parameters n_σ, F_{sat} and F_c are treated as tuneable. Following an initial sensitivity study to optimise the performance of the scheme (not shown), their values were set to $n_\sigma = 3$, $F_{sat} = 2$ and $F_c = 4$.

2.3 Data

AIRS (Aumann et al., 2003) is aboard the National Aeronautics and Space Administration's Aqua satellite, which was launched in May 2002. AIRS measures the thermal emissions of atmospheric constituents in the nadir and sub-limb observation geometry. An across-track scan consists of 90 individual footprints and covers a distance of 1765 km on the ground. The along-track distance between two scans is 18 km. The AIRS aperture is 1.1°, corresponding to a spatial resolution of 13.5 km at nadir and 41 km × 21.4 km at the scan extremes. The AIRS radiance measurements cover wavelength ranges from 3.74 to 15.4 µm with a total of 2378 radiance channels. The absolute error of the radiometric calibration is less than 0.2 %. The noise equivalent delta temperature is about 0.39 K at 250 K scene temperature for the spectral channel (666.5 cm^{-1}) considered here. The analyses presented in this paper are based on consolidated version 5 data products made freely available by NASA. The equatorial crossing of Aqua occurs at 13:30 LT (ascending orbit) and 01:30 LT (descending orbit). At high latitudes there is a quick transition between day- and night-time observations (e.g., Hoffmann et al., 2013). The Antarctic Peninsula is typically covered by four satellite overpasses per day. A more detailed description of AIRS is given in e.g. Hoffmann and Alexander (2009, 2010); Grimsdell et al. (2010); Hoffmann et al. (2013).

Infrared radiance measurements in the 4.3 and 15 µm CO_2 bands are of particular interest for the study of stratospheric gravity waves. These bands get optically thick in the stratosphere and as the CO_2 concentration does not vary substantially in the

ACPD
14, 18277–18314, 2014

lower and middle atmosphere, the radiance measurements in these channels are most sensitive to atmospheric temperature. Hoffmann and Alexander (2009) show the temperature kernel functions for the individual AIRS channels covering the 4.3 and 15 µm CO_2 bands. In this study we selected the 666.5 cm^{-1} radiance channel of AIRS, which is within the 15 µm CO_2 band. The temperature weighting function of this channel is given in Fig. 1, which shows that the brightness temperatures BT are most sensitive to atmospheric temperature at an altitude of 22 km, with full width at half maximum of 9 km. The altitude range covered by the 666.5 cm^{-1} channel is of particular interest for the formation of PSCs. As the kernel function drops to less than 1 % of maximum sensitivity below 14 km, there is little interference from tropospheric emissions from clouds or water vapour.

2.4 Methodology

Three instances of stratospheric mountain waves observed over the Antarctic Peninsula by AIRS, characterised by large amplitude and long vertical wavelength, occurred on 7 August 2011 at 03:40 UTC (case study 1, hereafter CS1), 2 August 2010 at 18:59 UTC (case study 2, hereafter CS2), and 14 July 2010 at 20:00 UTC (case study 3, hereafter CS3). These events were simulated by running the mesoscale model for a 48 h period driven by output from global model forecasts (following a 3 h spin-up) initialised on 5 August 2011 at 12:00 UTC for CS1, 1 August 2010 at 00:00 UTC for CS2, and 13 July 2010 at 00:00 UTC for CS3. The mesoscale model output times (integration time) closest to the actual measurement time are at 03:00 UTC on 7 August 2011 ($T + 39$ h) for CS1, at 19:00 UT on 2 August 2010 ($T + 43$ h) for CS2, and at 20:00 UT on 14 July 2010 ($T + 44$ h) for CS3 (note that for simplicity the mesoscale model integration times are given relative to the time of the global model initialisation). The output times reflect that the simulation of the mountain wave field requires at least a 24 h spin-up (Plougonven et al., 2010). Table 1 summarises this information. Figure 2 shows the near-surface (850 hPa) wind field simulated by the mesoscale model at the output time for each case study, showing that each of the mountain wave events were coin-

ACPD
14, 18277–18314, 2014

cident with strong westerly or north-westerly winds incident to the Peninsula. These winds showed the requisite strengthening with height required for the mountain waves to have long vertical wavelengths which were visible to AIRS (not shown).

To verify the mesoscale model forecasts, the Juelich Rapid Spectral Simulation Code (JURASSIC) radiative transfer model (Hoffmann and Alexander, 2009) was used to compute model simulated AIRS radiances at 666.5 cm^{-1}. For comparison, both the real and mesoscale model simulated AIRS radiances are subsequently converted into their corresponding BT values. Brightness temperature perturbations ΔBT were computed by removing a background brightness temperature, which was determined by fitting a 4th-order polynomial (e.g. Wu, 2004; Alexander and Barnet, 2007; Hoffmann and Alexander, 2010). This fit removes slowly varying atmospheric signals, e.g. from planetary waves and general scan-angle dependence of radiances due to the sub-limb geometry. For the AIRS measured radiances the fit was carried out for each scan in the across-track direction; for the mesoscale model simulated radiances it was carried out for each latitudinal band of the model grid. In both cases it was found that the fits are well constrained by the data and the process did not introduce any artificial wave-like structures that could obfuscate the results. In order to avoid the suppression of waves with fronts parallel to the fit direction the AIRS measured (simulated) background estimates were smoothed by a 300 km running mean in the along-track (longitudinal) direction. Finally, mesoscale model estimates of ΔBT are re-gridded to the AIRS measurement grid.

The mesoscale model forecasts were repeated using the climate model (i.e. the climate model is initialised using the same Met Office operational analysis and integrated forward in time for 48 h). Comparison of the mesoscale model and climate model simulations of the near-surface winds at the time of the mountain wave events (Fig. 2) shows relatively small differences in the large-scale flow impacting the Peninsula, i.e. the large-scale atmospheric conditions responsible for the initial forcing of the mountain waves are broadly similar in both models. As the mountain wave parameterisation scheme is implemented in the climate model, the temperature fluctuations predicted by

ACPD
14, 18277–18314, 2014

the scheme ΔT_{SSO}, as well as the temperature fluctuations explicitly resolved by the climate model ΔT_{CLIM} (computed by removing the background temperature, determined by fitting a 4th-order polynomial), can be assessed by comparing with those from the mesoscale model. Using the mesoscale model simulations enables investigation of the vertical profile of the parameterised output, in particular the vertical evolution of the wave phase, which is not possible at good vertical resolution using AIRS data alone. In the climate model implementation, ΔT_{SSO} is passed solely to the model output to enable its evaluation and is not used by the dynamical core or any other parameterisation scheme.

Finally, to assess the impact of the scheme on PSC microphysics and chemistry, perturbation and control experiments using the chemistry–climate model were conducted. In the perturbation experiments the mountain wave parameterisation is switched on. Following Carslaw et al. (1999), only the cooling phase ΔT^{-}_{SSO} of the parameterised temperature fluctuations are coupled to the PSC scheme, meaning that the warm phase is neglected. Carslaw et al. (1999) argue that this approach is physically justified as the warming phase of the wave-induced temperature fluctuations is typically of short enough duration that the complete evaporation of the PSC particles is unlikely to occur before temperatures fall again. In addition, evaporation will not occur if the synoptic-scale temperatures are sufficiently low that the warming phase still results in the temperature being below the PSC threshold value. The PSC scheme computes a "total" temperature, used only by itself, by combining the temperature explicitly resolved by the chemistry–climate model $T_{CHEM-CLIM}$ with ΔT^{-}_{SSO}. In the control experiment the mountain wave scheme is switched off. Both the perturbation and control experiments were run for 30 years (following a 30 year spin-up period) for a perpetual year-2000, using prescribed sea-surface temperatures and sea ice concentrations.

ACPD
14, 18277–18314, 2014

3 Mesoscale model verification

Figure 3 compares maps of measured and mesoscale model simulated estimates of ΔBT for each of the three case studies. In the left panels the measured field ΔBT_{AIRS} shows warm and cold temperature disturbances of amplitude 2–3 K clearly aligned with the western side of the Peninsula mountain ridge, i.e. typical of phase fronts associated with a mountain wave caused by low-level westerly flow passing over the Peninsula and propagating upward in the atmosphere. In the right panels the amplitude and structure of the corresponding mesoscale model field ΔBT_{MES} agrees well with the measurements.

Figure 4 compares ΔBT_{AIRS} and ΔBT_{MES} in more detail by examining their variation along the west–east orientated lines displayed in Fig. 3. The mountain wave appears prominently in both fields, with the mesoscale model producing a similar looking temperature disturbance to that measured. There are slight differences in terms of the wave amplitude, e.g. the mesoscale model amplitude in CS3 is slightly larger than that measured.

Note that in addition to a coherent mountain wave structure, Figs. 3 and 4 also show highly localised temperature fluctuations. For AIRS these fluctuations are partly due to increasing instrumental noise with low scene temperatures. The nominal noise of 0.39 K at 250 K scene temperature scales to 0.67–0.78 K at 190–200 K, which is more representative for the situations observed here.

4 Assessment of the mountain wave parameterisation

Having shown a very good comparison between measured and mesoscale model simulated ΔBT in the last section, we can now use the temperature fluctuations simulated by the mesoscale model ΔT_{MES} to assess the parameterised temperature fluctuations ΔT_{SSO}, as well as the temperature fluctuations explicitly resolved by the climate model ΔT_{CLIM}. However, due to the occurrence of spatially highly localised and strongly vary-

ACPD
14, 18277–18314, 2014

ing temperature fluctuations, the fairest approach is to compare profiles of ΔT_{SSO} and ΔT_{CLIM} for a particular N48 grid box with the mean and spread (± two standard deviations) of ΔT_{MES} for all the mesoscale model points within the same N48 grid box. This is shown in Fig. 5 for the N48 grid box centered at −70° latitude and −63.75° longitude, i.e. over the high-level ridge of the Antarctic Peninsula. The comparison shows that ΔT_{SSO} and the mean ΔT_{MES} response are generally in excellent agreement in terms of amplitude (which ranges from 5 to 10 K in the lower stratosphere), while ΔT_{SSO} and the mean ΔT_{MES} response are slightly out of alignment in terms of phase, evident by the maximum and minimum values of ΔT_{SSO} being roughly 1 km lower than those of the mean ΔT_{MES} response. However, at all altitudes ΔT_{SSO} lies within the spread ofΔT_{MES} (which reaches ±15 K in the lower stratosphere), suggesting that the parameterised temperature fluctuations are representative of the range of mesoscale model responses. Furthermore, the comparison shows that ΔT_{CLIM} completely fails to represent any temperature fluctuations, i.e. confirmation that the horizontal scale of the mountain waves are too small to be resolved by climate models, and hence their effects must be parameterised. Note that additional climate model runs at N96 resolution (192 × 145 grid points, or 1.875° × 1.25°) also completely failed to resolve any temperature fluctuations (not shown).

Figure 6 compares ΔT_{MES} and ΔT_{SSO} along a west-east cross section intersecting the Peninsula at −70° latitude. Only results for CS3 are shown as those for CS1 and CS2 were largely similar. The predominant feature of the ΔT_{MES} response is, as expected, a large-amplitude, vertically propagating mountain wave with phase lines tilting upstream with height, characterised by a horizontal wavelength of around 200 km, a vertical wavelength of around 15 km, and a amplitude of up to 15 K (in the lower stratosphere). It is clearly apparent that although the parameterisation scheme qualitatively captures the mesoscale model estimate of the temperature fluctuations in the lower stratosphere directly above the Peninsula, it: (i) fails to capture the upstream tilt of the phase lines, i.e. its phase lines are horizontal and do not tilt with height, and (ii) significantly underestimates the amplitude of the temperature fluctuations.

ACPD
14, 18277–18314, 2014

The lack of phase tilt is due to the parameterised wave field being represented by a hydrostatic gravity wave launched from an isolated bell-shaped ridge for each grid-box, which is then only propagated vertically through the column of air above. This simplification is also prohibitive in modelling the full downstream response. At N48 resolution the Antarctic Peninsula is multiple grid boxes wide as its resolved orography field is hugely smoothed/flattened (see Fig. 6) and is thus represented in the parameterisation as a series of very similar sub-grid ridges, while in the mesoscale model the Peninsula is resolved as a dominant wide single ridge. Therefore the parameterisation produces a simplified broad response, which has smaller amplitude compared to the mesoscale model, across the Peninsula, whereby any change in phase can only result from changes in U and N within each vertical column across the Peninsula. Further comparison of the mesoscale model and climate model simulations in Figs. 7 and 8 shows that with one exception (the lower altitude part of CS1) that U and N simulated by the climate model lie within the spread of the mesoscale model responses, i.e. indicating that the large-scale atmospheric conditions responsible for the parameterised phase evolution are representative of the range of mesoscale model responses. Furthermore, given its broad-scale response, it cannot be expected that the parameterised temperature fluctuations match the amplitude of the fine-scale fluctuations simulated by the mesoscale model. If the mesoscale model response would be spatially averaged the amplitudes would be in good agreement.

5 Impact of the mountain wave parameterisation on PSC formation

Having shown that the parameterised mountain wave-induced temperature fluctuations are broadly consistent with the mesoscale model results, we can progress to assessing the impact of including the wave-induced cooling phase $\Delta T^{-}_{\mathrm{SSO}}$ in the chemistry–climate model, again concentrating on the Antarctic Peninsula. In the first instance, we will examine the impact on the temperatures seen by the PSC scheme. Figure 9 shows for July at a height of 21 km the 30 year average difference in the frequency f

ACPD
14, 18277–18314, 2014

of the temperature falling below the 195 K and 188 K thresholds for PSC formation of type Ia and II, respectively. The differences are between the frequency based on the explicitly resolved temperature $T_{\mathrm{CHEM-CLIM}}$ plus $\Delta T^{-}_{\mathrm{SSO}}$ from the perturbation run, and the frequency based solely on the explicitly resolved temperature of the perturbation run, i.e. $f_{T_{\mathrm{CHEM-CLIM}}+\Delta T^{-}_{\mathrm{SSO}}} - f_{T_{\mathrm{CHEM-CLIM}}}$. The differences in frequency are always positive, which is consistent with only mountain wave cooling being used. The results show that over much of the Peninsula, the impact of the mountain wave cooling is to increase the frequency that the 195 K threshold is exceeded, peaking over its northern tip with a frequency difference of 4 percentage points. By comparison, the impact on the 188 K temperature threshold is even more dramatic, resulting in differences which are both larger and extending much further south, peaking over Alexander Island to the south-west of the Peninsula with a frequency difference of over 6 percentage points. The fact that the differences in 195 K threshold frequency are located predominately over the middle and northern sections of the Peninsula is consistent with the climatological 195 K isotherm of the perturbation run being situated at approximately −75° latitude (not shown). Hence, any increase in the frequency of temperatures falling below 195 K as a result of the parameterisation can only occur northward of this, i.e. where the large-scale temperature is not already less than 195 K. Similarly, the differences in 188 K threshold frequency which encompass the entire length of the Peninsula are consistent with the model 188 K isotherm being situated southward of the 195 K isotherm (not shown). Figure 10 compares the 30 year temperature distribution based on $T_{\mathrm{CHEM-CLIM}} + \Delta T^{-}_{\mathrm{SSO}}$ of the perturbation run against that of $T_{\mathrm{CHEM-CLIM}}$ for the perturbation run for the same N48 grid box used for Figs. 5, 7 and 8, again for July and at 21 km. As expected, inclusion of the parameterised mountain wave cooling shifts the temperature distribution to lower temperatures. In particular, it causes a longer left tail of the temperature distribution which extends down to 177 K (or 5 K colder than the temperature distribution based solely on $T_{\mathrm{CHEM-CLIM}}$).

The effect of the parameterisation on PSCs is investigated by evaluating the 30 year average difference in PSC surface area density between the perturbation and control

ACPD
14, 18277–18314, 2014

simulations (perturbation minus control). PSC surface area density controls the amount of reactive chlorine species produced, which cause ozone destruction. Figure 11 shows the difference in PSC surface area density at a height of 21 km for July. The perturbation run results in increases in surface area density for all PSCs (i.e. combined type I and II) of 6–10 $\mu m^2\,cm^{-3}$ over the Antarctic Peninsula and $> 10\,\mu m^2\,cm^{-3}$ over the Bellingshausen Sea. Relative to the control run, these are equivalent to increases of more than 50 % over the northern tip of the Antarctic Peninsula, and at least 30 % over the Bellingshausen Sea. The Weddell Sea region shows a non-significant decrease in PSC surface area density. This is not unexpected, even though the first order expectation is for a large-area increase in PSCs. The chemistry–climate model is interactive: changing PSCs change chlorine activation, which impacts ozone loss. Changing ozone alters the heating rates that impact temperatures and circulation. What is diagnosed in Fig. 11 (and related figures) is the difference between two climate equilibrium states for identical boundary conditions (compare e.g. Braesicke et al., 2013). Consequently, what is shown in the figures is locally strongly influenced by the additional parameterisation (adding localised cooling and thus producing more PSCs), but in regions away from the direct impact the response can be determined by feedback mechanisms. Figure 11 additionally separates these differences into their individual contributions from type I and type II PSCs. It is type I (type II) PSCs which are largely responsible for the overall PSC increase over the Antarctic Peninsula (Bellingshausen Sea). Note that significant differences in PSC surface area density were also evident in June, but not in August and September (not shown).

6 Summary and discussion

This study demonstrates that: (i) UM high-resolution (4 km) mesoscale model simulations are able to accurately simulate the large mountain wave-induced temperature fluctuations in the lower stratosphere associated with strong westerly or north-westerly flow over the Antarctic Peninsula, and (ii) UM low-resolution ($2.5^\circ \times 3.75^\circ$) climate model

ACPD
14, 18277–18314, 2014

simulations are completely unable to resolve such temperature fluctuations. These fluctuations act as a significant source of localised PSC formation as they enable stratospheric temperatures which otherwise would remain above the temperature threshold for PSC formation, to fall below it. With low spatial resolution a model is unable to resolve such temperature fluctuations, and as a consequence underestimate mountain wave-induced PSCs and the attendant PSC-induced ozone depletion. This in turn is also a good rational for using the negative temperature anomalies only for the call to the chemistry scheme. On a sub-grid scale, going below a threshold temperature will produce additional PSCs, whereas staying above will not trigger PSCs. So for a grid-box averaged PSC coverage only additional incidents below the threshold temperature increase the coverage. Certainly for such an assumption to be true the sub-grid wave train should be slowly evolving horizontally compared to the model time step, thus producing an additional PSC occurrence frequency on the fringes of the synoptic-scale threshold temperature regions, as has been illustrated with Fig. 9 and discussed above.

To investigate the impact of temperature fluctuations due to unresolved (sub-grid scale) mountain waves the parameterisation of Dean et al. (2007) was implemented in the UM climate model. It describes the vertical evolution of a linear hydrostatic wave forced by steady, stably stratified flow over a two-dimensional ridge. By determining the vertical evolution of the wave amplitude and the wave phase (alternative schemes such as Wells et al. (2011) solely compute the wave amplitude), the parameterisation is able to calculate the maximum downward and upward vertical displacement and subsequently the associated positive and negative temperature fluctuations. Its performance was assessed against the mesoscale model simulations. This comparison demonstrated that: (i) the parameterised temperature fluctuations lie within the spread of the mesoscale model response, and (ii) the amplitude and phase of the parameterised temperature fluctuations are broadly in agreement with the mean mesoscale model response. However, the comparison also showed that the parameterisation cannot represent the upstream tilt of the phase lines with height, which is characteristic of a coherent hydrostatic mountain wave, due to it representing the Peninsula by a series

ACPD
14, 18277–18314, 2014

of independent sub-grid scale ridges which each launch a mountain wave vertically through the column of air above. Moreover, the parameterisation also does not represent trapped mountain lee waves, which can result in localised cooling many hundreds of kilometres downstream (e.g. Dörnbrack et al., 1999).

The study followed this by assessing the impact on PSCs using the UKCA chemistry–climate model. It was found that adding the wave-induced cooling phase to the resolved temperature had a substantial impact on the frequency and magnitude of low temperatures which satisfy PSC thresholds, resulting in a regional 30–50 % increase in PSC surface area density during July at a height of 21 km over the Antarctic Peninsula and the Bellingshausen Sea. It should be stressed that we were unable to compare these results with observations as: (i) detailed measurements of Antarctic PSCs over a decadal time scale are not available at present (Austin et al., 2010), and (ii) global atmospheric reanalyses do not resolve small-scale temperature fluctuations. Our decision to neglect the wave-induced warming phase might imply that the diagnosed increase should perhaps be considered as an upper bound. However, as mentioned above, the formation of PSCs downstream due to trapped lee waves is currently not represented in the model. Carslaw et al. (1999) remedied this by applying a horizontal "influence function" to simulate cooling downstream of orography, and a similar approach will be considered in future implementations of the scheme in UKCA chemistry–climate model. The simulation of PSC differences both upstream and downstream of the Antarctic Peninsula, and hence removed from the actual region where the parameterisation impacts temperatures directly, is suggestive of a new climate-equilibrium state being established in the model that allow non-local effects to occur. Investigation of this will be the subject of future study. Moreover, the parameterisation might offer a method for improving lower stratospheric model temperatures that more often satisfy conditions for PSC formation, the failure of which was suggested by Austin et al. (2010) to be one of the main reasons for the poor simulation of ozone depletion.

It is worth noting that other biases can affect the ability of chemistry–climate models to realistically simulate PSCs. For example, the failure of many models to represent the

ACPD
14, 18277–18314, 2014

effects of non-orographic gravity wave drag can result in unrealistically cold temperatures in the Southern Hemisphere winter stratosphere (Orr et al., 2010), i.e. resulting in synoptic-scale temperatures which fall below the PSC temperature threshold when in reality they should be above it, which as a consequence cause the formation of too many PSCs and associated increased ozone losses (Austin et al., 2003). Moreover, the standard quasi-equilibrium PSC scheme used by the UKCA module does not advect PSC particles (Feng et al., 2011), i.e. the impact on PSC formation of the mountain wave parameterisation scheme is localised to wherever the temperature fluctuations are applied. This means that the occurrence of circumpolar belts of PSCs which have been attributed to mountain wave-induced PSCs over regions such as the Antarctic Peninsula would not be represented. However, future work will investigate replacing the quasi-equilibrium PSC scheme with the full microphysical scheme DLAPSE (Denitrification by Lagrangian Particle Sedimentation), which uses a Lagrangian trajectory scheme and as such is able to transport PSC particles away from the region of formation (Feng et al., 2011). However, the current study illustrates that a more comprehensive treatment of sub-grid scale mountain waves in a global climate model leads to realistic localised temperature change diagnostics. Subsequently, we have been able to assess and characterise the localised impact of the modelled temperature fluctuations in a comprehensive chemistry–climate model. Further work will investigate the non-localised effects in more detail.

Acknowledgements. The authors thank T. Phillips for providing much assistance in producing the figures. This study is part of the British Antarctic Survey Polar Science for Planet Earth Programme. It was funded by The Natural Environment Research Council (grant number NE/H022988/1). AIRS data are distributed by NASA Goddard Earth Science Data Information and Services Center. This work made use of the facilities HECToR, the UK's national high-performance computing service, which is provided by UoE HPCx Ltd at the University of Edinburgh, Cray Inc and NAG Ltd, and funded by the Office of Science and Technology through EPSRC's High End Computing Programme.

ACPD
14, 18277–18314, 2014

References

Alfred, J., Fromm, M., Bevilacqua, R., Nedoluha, G., Strawa, A., Poole, L., and Wickert, J.: Observations and analysis of polar stratospheric clouds detected by POAM III and SAGE III during the SOLVE II/VINTERSOL campaign in the 2002/2003 Northern Hemisphere winter, Atmos. Chem. Phys., 7, 2151–2163, doi:10.5194/acp-7-2151-2007, 2007.

Alexander, J. M. and Barnet, C. D.: Using satellite observations to constrain gravity wave parameterizations for global models, J. Atmos. Sci., 64, 1652–1665, doi:10.1175/JAS3897.1, 2007.

Alexander, J. M. and Teitelbaum, H.: Observation and analysis of a large amplitude mountain wave event over the Antarctic Peninsula, J. Geophys. Res., 112, D21103, doi:10.1029/2006JD008368, 2007.

Alexander, S. P., Klekociuk, A. R., Pitts, M. C., McDonald, A. J., and Arevalo-Torres, A.: The effect of orographic gravity waves on Antarctic polar stratospheric cloud occurrence and composition, J. Geophys. Res., 116, D06109, doi:10.1029/2010JD015184, 2011.

Alexander, S. P., Klekociuk, A. R., McDonald, A. J., and Pitts, M. C.: Quantifying the role of orographic gravity waves on polar stratospheric cloud occurrence in the Antarctic and the Arctic, J. Geophys. Res., 118, 11493–11507, doi:10.1002/2013JD020122, 2013.

Aumann, H. H., Chahine, M. T., Gautier, C., Goldberg, M. D., Kalnay, E., McMillin, L. M., Revercomb, H., Rosenkranz, P. W., Smith, W. L., Staelin, D. H., Strow, L. L., and Susskind, J.: AIRS/AMSU/HSB on the Aqua mission: design, science objective, data products, and processing systems, IEEE T. Geosci. Remote, 41, 253–264, doi:10.1109/TGRS.2002.808356, 2003.

Austin, J. and Butchart, N.: Coupled chemistry–climate model simulations for the period 1980 to 2020: ozone depletion and the start of ozone recovery, Q. J. Roy. Meteor. Soc., 129, 3225–3249, doi:10.1256/qj.02.203, 2003.

Austin, J., Struthers, H., Scinocca, J., Plummer, D. A., Akiyoshi, H., Baumgaertner, A. J. G., Bekki, S., Bodeker, G. E., Braesicke, P., Brühl, C., Butchart, N., Chipperfield, M. P., Cugnet, D., Dameris, M., Dhomse, S., Frith, S., Garny, H., Gettelman, A., Hardiman, S. C., Jöckel, P., Kinnison, D., Kubin, A., Lamarque, J. F., Langematz, U., Mancini, E., Marchand, M., Michou, M., Morgenstern, O., Nakamura, T., Nielsen, J. E., Pitari, G., Pyle, J., Rozanov, E., Shepherd, T. G., Shibata, K., Smale, D., Teyssèdre, H., and Yamashita, Y.:

ACPD
14, 18277–18314, 2014

Chemistry–climate model simulations of spring Antarctic ozone, J. Geophys. Res., 115, D00M11, doi:10.1029/2009JD013577, 2010.
Braesicke, P., Keeble, J., Yang, X., Stiller, G., Kellmann, S., Abraham, N. L., Archibald, A., Telford, P., and Pyle, J. A.: Circulation anomalies in the Southern Hemisphere and ozone changes, Atmos. Chem. Phys., 13, 10677–10688, doi:10.5194/acp-13-10677-2013, 2013.
Campbell, J. R. and Sassen, K.: Polar stratospheric clouds at the South Pole from 5 years of continuous lidar data: macrophysical, optical, and thermodynamic properties, J. Geophys. Res., 113, D20204, doi:10.1029/2007JD009680, 2008.
Cariolle, D., Muller, S., Cayla, F., and McCormick, M. P.: Mountain waves, polar stratospheric clouds, and ozone depletion over Antarctica, J. Geophys. Res., 94, 11233–11240, doi:10.1029/JD094iD09p11233, 1989.
Carslaw, K. S., Wirth, M., Tsias, A., Luo, B. P., Dörnbrack, A., Leutbecher, M., Volkert, H., Renger, W., Bacmeister, J. T., and Peter, T.: Particle microphysics and chemistry in remotely observed mountain polar stratospheric clouds, J. Geophys. Res., 103, 5785–5796, doi:10.1029/97JD03626, 1998a.
Carslaw, K. S., Wirth, M., Tsias, A., Luo, B. P., Dörnbrack, A., Leutbecher, M., Volkert, H., Renger, W., Bacmeister, J. T., Reimer, E., and Peter, T.: Increased stratospheric ozone depletion due to mountain-induced atmospheric waves, Nature, 391, 675–678, 1998b.
Carslaw, K. S., Peter, T., Bacmeister, J. T., and Eckermann, S. D.: Widespread solid particle formation by mountain waves in the Arctic stratosphere, J. Geophys. Res., 104, 1827–1836, doi:10.1029/1998JD100033, 1999.
Dean, S. M., Flowerdew, J., Lawrence, B. N., and Eckermann, S. D.: Parameterisation of orographic cloud dynamics in a GCM, Clim. Dynam., 28, 581–597, doi:10.1007/s00382-006-0202-0, 2007.
Donlon, C. J., Martin, M., Stark, J. D., Roberts-Jones, J., Fiedler, E., and Wimmer, W.: The Operational Sea Surface Temperature and Sea Ice analysis (OSTIA), Remote Sens. Environ., 116, 140–158, doi:10.1016/j.rse.2010.10.017, 2011.
Dörnbrack, A. and Leutbecher, M.: Relevance of mountain waves for the formation of polar stratospheric clouds over Scandinavia: a 20 year climatology, J. Geophys. Res., 106, 1583–1593, doi:10.1029/2000JD900250, 2001.
Dörnbrack, A., Leutbecher, M., Kivi, R., and Kyrö, E.: Mountain-wave-induced record low stratospheric temperatures above northern Scandinavia, Tellus A, 51, 951–963, 1999.

ACPD
14, 18277–18314, 2014

Dörnbrack, A., Birner, T., Fix, A., Flentje, H., Meister, A., Schmid, H., Browell, E. V., and Mahoney, M. J.: Evidence for inertia gravity waves forming in polar stratospheric clouds over Scandinavia, J. Geophys. Res., 107, 8287, doi:10.1029/2001JD000452, 2002.

Dörnbrack, A., Pitts, M. C., Poole, L. R., Orsolini, Y. J., Nishii, K., and Nakamura, H.: The 2009–2010 Arctic stratospheric winter – general evolution, mountain waves and predictability of an operational weather forecast model, Atmos. Chem. Phys., 12, 3659–3675, doi:10.5194/acp-12-3659-2012, 2012.

Eckermann, S. D., Hoffmann, L., Höpfner, M., Wu, D. L., and Alexander, M. J.: Antarctic NAT PSC belt of June 2003: observational validation of the mountain wave seeding hypothesis, Geophys. Res. Lett., 36, L02807, doi:10.1029/2008GL036629, 2009.

Eyring, V., Butchart, N., Waugh, D. W., Akiyoshi, H., Austin, J., Bekki, S., Bodeker, G. E., Boville, B. A., Brühl, C., Chipperfield, M. P., Cordero, E., Dameris, M., Deushi, M., Fioletov, V. E., Frith, S. M., Garcia, R. R., Gettelman, A., Giorgetta, M. A., Grewe, V., Jourdain, L., Kinnison, D. E., Mancini, E., Manzini, E., Marchand, M., Marsh, D. R., Nagashima, T., Newman, P. A., Nielsen, J. E., Pawson, S., Pitari, G., Plummer, D. A., Rozanov, E., Schraner, M., Shepherd, T. G., Shibata, K., Stolarski, R. S., Struthers, H., Tian, W., and Yoshiki, M.: Assessment of temperature, trace species and ozone in chemistry–climate model simulations of the recent past, J. Geophys. Res., 111, D22308, doi:10.1029/2006JD007327, 2006.

Eyring, V., Arblaster, J. M., Cionni, I., Sedláèek, J., Perlwitz, J., Young, P. J., Bekki, S., Bergmann, D., Cameron-Smith, P., Collins, W. J., Faluvegi, G., Gottschaldt, K.-D., Horowitz, L. W., Kinnison, D. E., Lamarque, J.-F., Marsh, D. R., Saint-Martin, D., Shindell, D. T., Sudo, K., Szopa, S., and Watanabe, S.: Long-term ozone changes and associated climate impacts in CMIP5 simulations, J. Geophys. Res., 118, 5029–5060, doi:10.1002/jgrd.50316, 2013.

Feng, W., Chipperfield, M. P., Davies, S., Mann, G. W., Carslaw, K. S., Dhomse, S., Harvey, L., Randall, C., and Santee, M. L.: Modelling the effect of denitrification on polar ozone depletion for Arctic winter 2004/2005, Atmos. Chem. Phys., 11, 6559–6573, doi:10.5194/acp-11-6559-2011, 2011.

Grimsdell, A. W., Alexander, M. J., May, P. T., and Hoffmann, L.: Model study of waves generated by convection with direct validation via satellite, J. Atmos. Sci., 67, 1617–1631, doi:10.1175/2009JAS3197.1, 2010.

Hewitt, H. T., Copsey, D., Culverwell, I. D., Harris, C. M., Hill, R. S. R., Keen, A. B., McLaren, A. J., and Hunke, E. C.: Design and implementation of the infrastructure of

ACPD
14, 18277–18314, 2014

HadGEM3: the next-generation Met Office climate modelling system, Geosci. Model Dev., 4, 223–253, doi:10.5194/gmd-4-223-2011, 2011.
Hoffmann, L. and Alexander, M. J.: Retrieval of stratospheric temperatures from Atmospheric Infrared Sounder radiance measurements for gravity wave studies, J. Geophys. Res., 114, D07105, doi:10.1029/2008JD011241, 2009.
Hoffmann, L. and Alexander, M. J.: Occurrence frequency of convective gravity waves during the North American thunderstorm season, J. Geophys. Res., 115, D20111, doi:10.1029/2010JD014401, 2010.
Hoffmann, L., Xue, X., and Alexander, M. J.: A global view of stratospheric gravity wave hotspots located with Atmospheric Infrared Sounder observations, J. Geophys. Res., 118, 416–434, doi:10.1029/2012JD018658, 2013.
Höpfner, M., Larsen, N., Spang, R., Luo, B. P., Ma, J., Svendsen, S. H., Eckermann, S. D., Knudsen, B., Massoli, P., Cairo, F., Stiller, G., v. Clarmann, T., and Fischer, H.: MIPAS detects Antarctic stratospheric belt of NAT PSCs caused by mountain waves, Atmos. Chem. Phys., 6, 1221–1230, doi:10.5194/acp-6-1221-2006, 2006.
Jensen, E. J., Toon, O., Tabazadeh, A., and Drdla, K.: Impact of polar stratospheric cloud particle composition, number density, and lifetime on denitrification, J. Geophys. Res., 107, 8284, doi:10.1029/2001JD000440, 2002.
Liu, H., Jezek, K., Li, B., and Zhao, Z.: Radarsat Antarctic Mapping Project Digital Elevation Model Version 2, National Snow and Ice Data Center, Boulder, Colorado, 2001.
Lott, F. and Miller, M.: A new subgrid scale orographic drag parameterization; its testing in the ECMWF model, Q. J. Roy. Meteor. Soc., 123, 101–127, doi:10.1002/qj.49712353704, 1997.
Noel, V. and Pitts, M.: Gravity wave events from mesoscale simulations, compared to polar stratospheric clouds observed from spaceborne lidar over the Antarctic Peninsula, J. Geophys. Res., 117, D11207, doi:10.1029/2011JD017318, 2012.
Noel, V., Hertzog, A., and Chepfer, H.: CALIPSO observations of wave-induced PSCs with near-unity optical depth over Antarctica in 2006–2007, J. Geophys. Res., 114, D05202, doi:10.1029/2008JD010604, 2009.
McDonald, A. J., George, S. E., and Woollands, R. M.: Can gravity waves significantly impact PSC occurrence in the Antarctic?, Atmos. Chem. Phys., 9, 8825–8840, doi:10.5194/acp-9-8825-2009, 2009.

ACPD
14, 18277–18314, 2014

McFarlane, N. A.: The effect of orographically excited gravity wave drag on the general circulation of the lower stratosphere and troposphere, J. Atmos. Sci., 44, 1775–1800, doi:10.1175/1520-0469(1987)044<1775:TEOOEG>2.0.CO;2, 1987.

Morgenstern, O., Braesicke, P., O'Connor, F. M., Bushell, A. C., Johnson, C. E., Osprey, S. M., and Pyle, J. A.: Evaluation of the new UKCA climate-composition model – Part 1: The stratosphere, Geosci. Model Dev., 2, 43–57, doi:10.5194/gmd-2-43-2009, 2009.

Morgenstern, O., Giorgetta, M. K., Shibata, K., Eyring, V., Waugh, D. W., Shepherd, T. G., Akiyoshi, H., Austin, J., Baumgaertner, A. J. G., Bekki, S., Braesicke, P., Brühl, C., Chipperfield, M. P., Cugnet, D., Dameris, M., Dhomse, S., Frith, S. M., Garny, H., Gettelman, S., Hardiman, S. C., Hegglin, M. I., Jöckel, P., Kinnison, D. E., Lamarque, J.-F., Mancini, E., Manzini, E., Marchand, M., Michou, M., Nakamura, T., Nielsen, J. E., Olivié, D., Pitari, G., Plummer, D. A., Rozanov, E., Scinocca, J. F., Smale, D., Teyssèdre, H., Toohey, M., Tian, W., and Yamashita, Y.: Review of the formulation of present-generation stratospheric chemistry–climate models and associated external forcings, J. Geophys. Res., 115, D00M02, doi:10.1029/2009JD013728, 2010.

Orr, A., Marshall, G., Hunt, J. C. R., Sommeria, J., Wang, C., van Lipzig, N., Cresswell, D., and King, J. C.: Characteristics of airflow over the Antarctic Peninsula and its response to recent strengthening of westerly circumpolar winds, J. Atmos. Sci., 65, 1396–1413, doi:10.1175/2007JAS2498.1, 2008.

Orr, A., Bechtold, P., Scinocca, J., Ern, M., and Janiskova, M.: Improved middle atmosphere climate and forecasts in the ECMWF model through a nonorographic gravity wave drag parameterization, J. Climate, 5905–5926, doi:10.1175/2010JCLI3490.1, 2010.

Orr, A., Bracegirdle, T. J., Hoskings, J. S., Jung, T., Haigh, J. D., Phillips, T., and Feng, W.: Possible dynamical mechanisms for Southern Hemisphere climate change due to the ozone hole, J. Atmos. Sci., 69, 2917–2932, doi:10.1175/JAS-D-11-0210.1, 2012.

Orr, A., Phillips, T., Webster, S., Elvidge, A., Weeks, M., Hosking, J. S., and Turner, J.: Met Office Unified Model high resolution simulations of a strong wind event in Antarctica, Q. J. Roy. Meteor. Soc., doi:10.1002/qj.2296, 2014.

Pawson, S., Naujokat, B., and Labitzke, K.: On the polar stratospheric cloud formation potential of the northern stratosphere, J. Geophys. Res., 100, 23215–23225, doi:10.1029/95JD01918, 1995.

ACPD
14, 18277–18314, 2014

Plougonven, R., Hertzog, A., and Teitelbaum, H.: Observations and simulations of large-amplitude mountain wave breaking over the Antarctic Peninsula, J. Geophys. Res., 113, D16113, doi:10.1029/2007JD009739, 2008.

Plougonven, R., Arsac, A., Hertzong, A., Guez, L., and Vial, F.: Sensitivity study for mesoscale simulations of gravity waves above Antarctica during Vorcore, Q. J. Roy. Meteor. Soc., 136, 1371–1377, doi:10.1002/qj.639, 2010.

Polvani, L. M., Previdi, M., and Deser, C.: Large cancellation, due to ozone recovery, of future Southern Hemisphere atmospheric circulation trends, Geophys. Res. Lett., 38, L04707, doi:10.1029/2011GL046712, 2011.

Reinecke, P. and Durran, D. R.: The over-amplification of gravity waves in numerical solutions to flow over topography, Mon. Weather Rev., 137, 1533–1549, doi:10.1175/2008MWR2630.1, 2009.

Solomon, S.: Stratospheric ozone depletion: a review of concepts and history, Rev. Geophys., 37, 275–316, doi:10.1029/1999RG900008, 1999.

SPARC: SPARC Report on the Lifetimes of Stratospheric Ozone-Depleting Substances, Their Replacements, and Related Species, edited by: Ko, M., Newman, P., Reimann, S., Strahan, S., SPARC Report No. 6, WCRP-15/2013, 2013.

Thompson, D. W. J., Solomon, S., Kushner, P. J., England, M. H., Grise, K. M., and Karoly, D. J.: Signatures of the Antarctic ozone hole in Southern Hemisphere surface climate change, Nat. Geosci., 4, 741–749, 2011.

Webster, S., Uddstrom, M., Oliver, H., and Vosper, S.: A high-resolution modelling case study of a severe weather event over New Zealand, Atmos. Sci. Lett., 9, 119–128, doi:10.1002/asl.172, 2008.

Wells, H., Vosper, S. B., and Yan, X.: An assessment of a mountain-wave parametrization scheme using satellite observations of stratospheric gravity waves, Q. J. Roy. Meteor. Soc., 137, 819–828, doi:10.1002/qj.790, 2011.

Wu, D. L.: Mesoscale gravity wave variances from AMSU-A radiances, Geophys. Res. Lett., 31, L12114, doi:10.1029/2004GL019562, 2004.

Wu, D. L. and Eckermann, S. D.: Global gravity wave variances from Aura MLS: characteristics and interpretation, J. Atmos. Sci., 65, 3695–3718, doi:10.1175/2008JAS2489.1, 2008.

ACPD
14, 18277–18314, 2014

Table 1. Dates and times of the three mountain wave case studies for the AIRS measurements, the start of the mesoscale and climate model simulations, and the model forecast/output nearest the AIRS measurements (in UTC).

Case study	AIRS measurement	Model start	Model output time nearest the AIRS measurement
CS1	7 Aug 2011, 03:40	5 Aug 2011, 12:00	7 Aug 2011, 03:00 ($T + 39$ h)
CS2	2 Aug 2010, 18:59	1 Aug 2010, 00:00	2 Aug 2010, 19:00 ($T + 43$ h)
CS3	14 Jul 2010, 20:00	13 Jul 2010, 00:00	14 Jul 2010, 20:00 ($T + 44$ h)

ACPD
14, 18277–18314, 2014

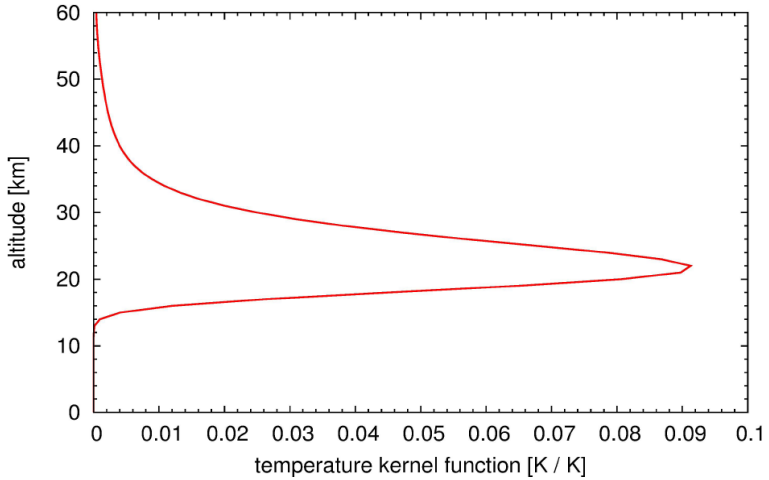

Figure 1. The temperature weighting function (brightness temperature (K)/temperature (K)) for the 666.5 cm^{-1} AIRS channel. This function was calculated for a polar winter reference atmosphere, a 1 km altitude grid, and the nadir observation geometry.

ACPD
14, 18277–18314, 2014

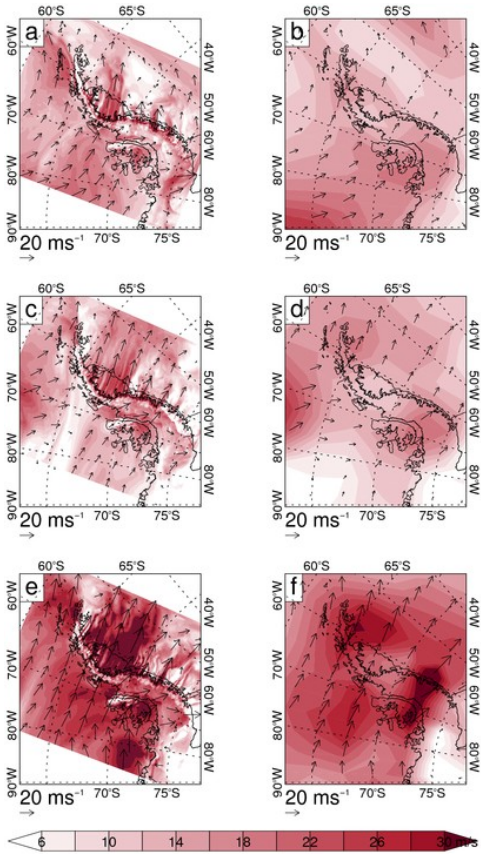

Figure 2. Mesoscale model (left) and climate model (right) simulation of the 850 hPa wind field ($m\,s^{-1}$) over the Antarctic Peninsula at the time of the CS1 **(a, b)**, CS2 **(c, d)**, and CS3 **(e, f)** mountain wave events. See Table 1 for dates. The black arrows are wind vectors (for the mesoscale model only 1 in every 40 grid points is shown). The colour shading indicates the wind magnitude. Also shown is the coastline of the Antarctic Peninsula.

ACPD
14, 18277–18314, 2014

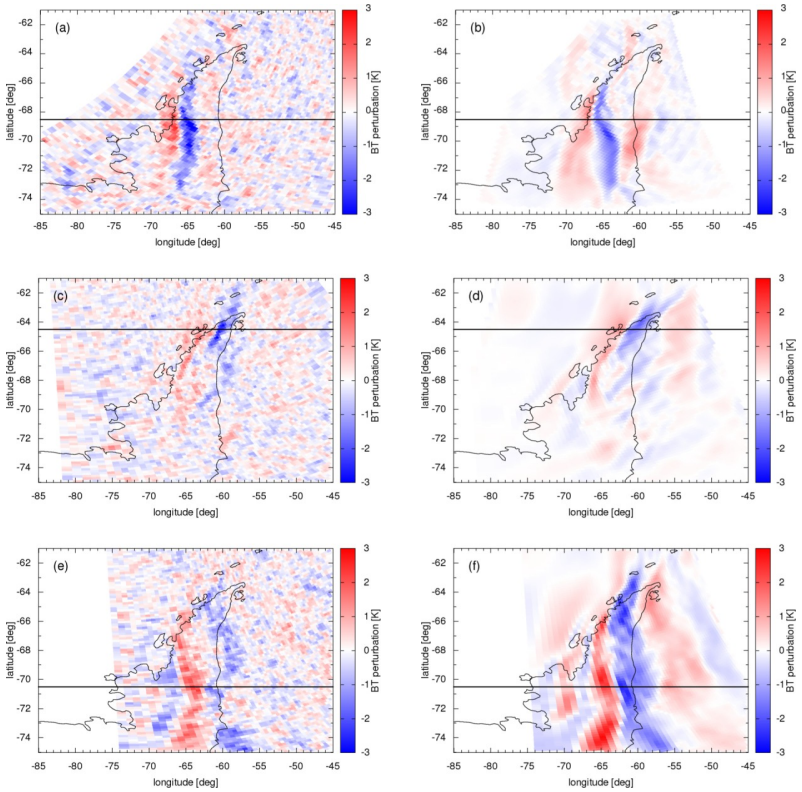

Figure 3. Measured (left) and mesoscale model (right) estimates of brightness temperature perturbations (K) corresponding to the 666.5 cm^{-1} AIRS channel at the time of the CS1 **(a, b)**, CS2 **(c, d)**, and CS3 **(e, f)** mountain wave events. See Table 1 for dates. The horizontal black lines indicate the latitude band selected for a more detailed comparison, shown in Fig. 4. Also shown is the coastline of the Antarctic Peninsula.

ACPD
14, 18277–18314, 2014

Inclusion of mountain wave-induced cooling

A. Orr et al.

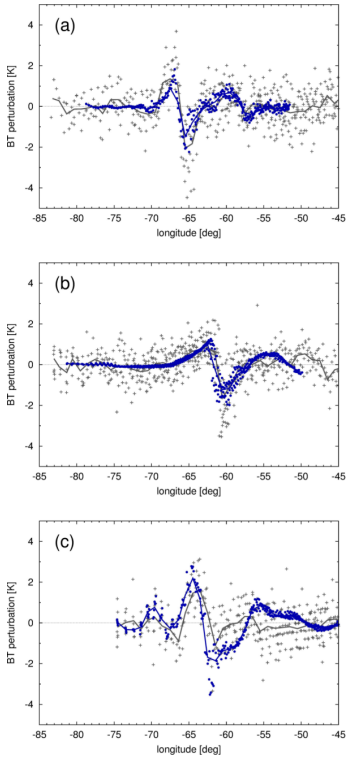

Figure 4. Measured (gray) and mesoscale model simulated (blue) brightness temperature fluctuations (K) corresponding to the 666.5 cm^{-1} AIRS channel along a latitude band intersecting the Antarctic Peninsula (indicated on Fig. 3) at the time of the CS1 **(a)**, CS2 **(b)**, and CS3 **(c)** mountain wave events. See Table 1 for dates. Model data have been re-sampled on the AIRS measurement grid. Note that the model domain does not always cover the full AIRS swath, therefore re-gridded model data are missing at some longitudes in CS1 and CS2. The solid lines show a 1° running mean in longitude of the individual temperature fluctuations.

ACPD
14, 18277–18314, 2014

Inclusion of mountain wave-induced cooling

A. Orr et al.

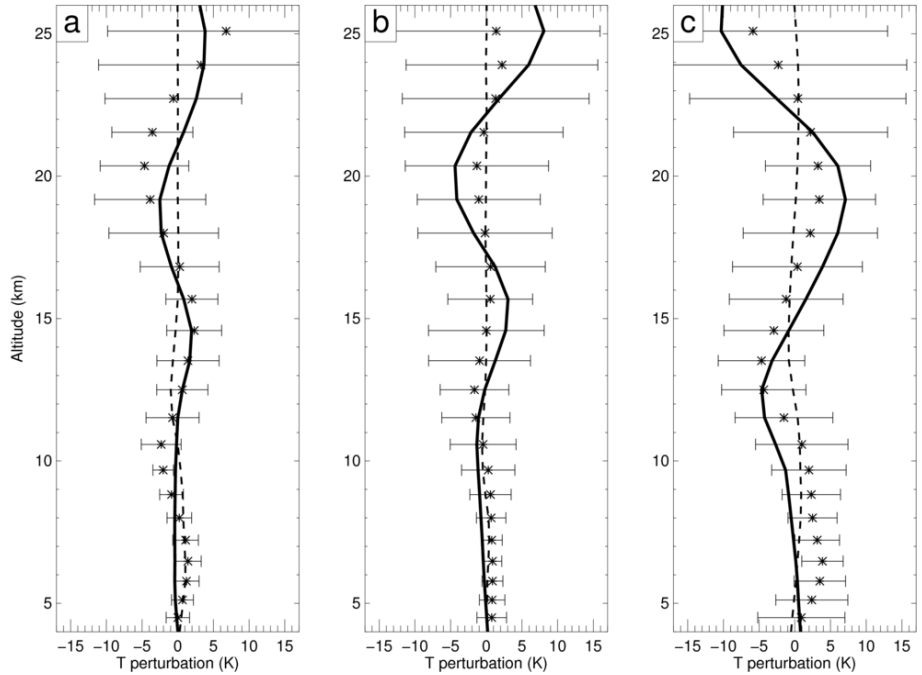

Figure 5. Vertical profile of temperature fluctuations (K) resolved by the climate model (dashed line), resolved by the mesoscale model (stars and horizontal bars), and parameterised by the mountain wave scheme (solid line) at the time of the CS1 **(a)**, CS2 **(b)**, and CS3 **(c)** mountain wave events. See Table 1 for dates. The temperature fluctuations resolved by the climate model and parameterised by the scheme are for the N48 grid box centered on −70° latitude and −63.75° longitude, i.e. over the high-elevation ridge of the Antarctic Peninsula. The mesoscale model temperature fluctuations are the mean (stars) and spread (± two standard deviations, horizontal bars) of all the mesoscale model points within the same N48 grid box.

ACPD
14, 18277–18314, 2014

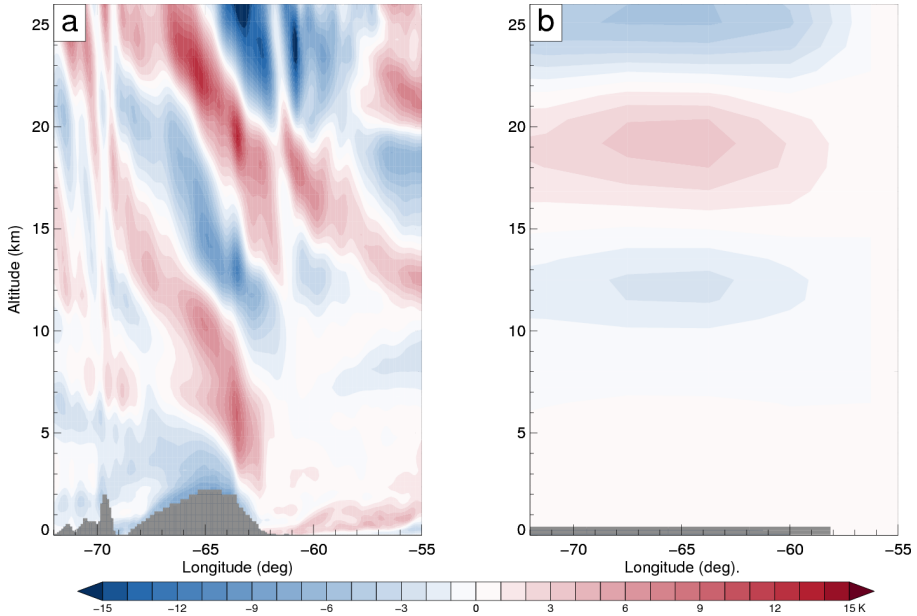

Figure 6. Vertical cross section intersecting the Antarctic Peninsula along a latitude band at −70° of the temperature fluctuation (K) simulated by the mesoscale model **(a)** and the mountain wave parameterisation **(b)** at the time of the CS3 mountain wave event. See Table 1 for dates. The grey shading indicates the height of the explicitly resolved orography.

ACPD
14, 18277–18314, 2014

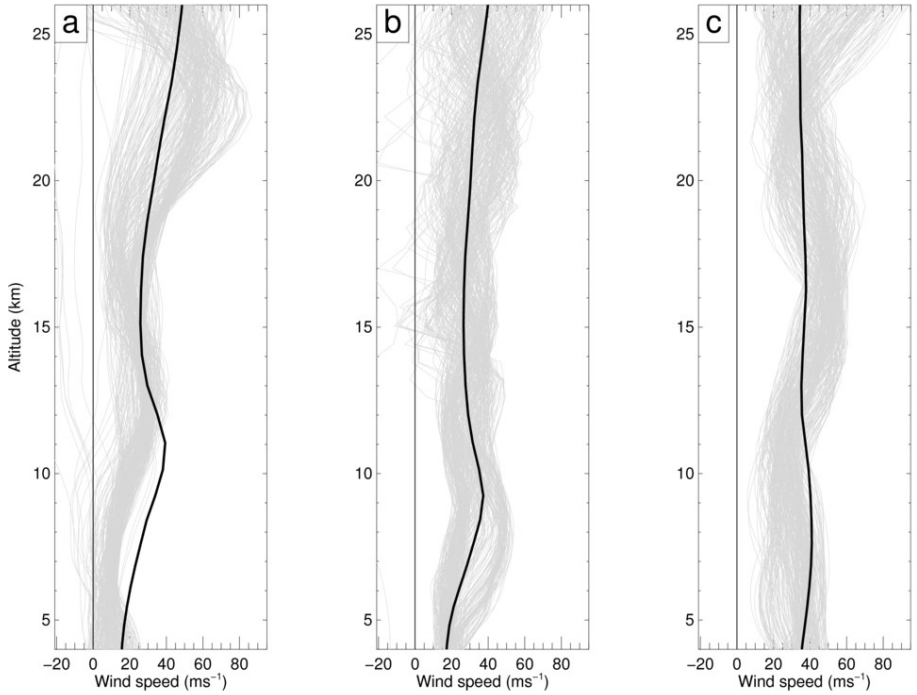

Figure 7. Vertical profile of the wind speed *U* (resolved in the direction of the wave vector, which is taken to be the direction of the 850 hPa wind vector) simulated by the climate model (black line) and the mesoscale model (grey lines) at the time of the CS1 **(a)**, CS2 **(b)**, and CS3 **(c)** mountain wave events. See Table 1 for dates. The climate model profile is from the same N48 grid box (i.e. over the high-elevation ridge of the Antarctic Peninsula). The mesoscale model profiles are for all the mesoscale model points within the N48 grid box.

ACPD
14, 18277–18314, 2014

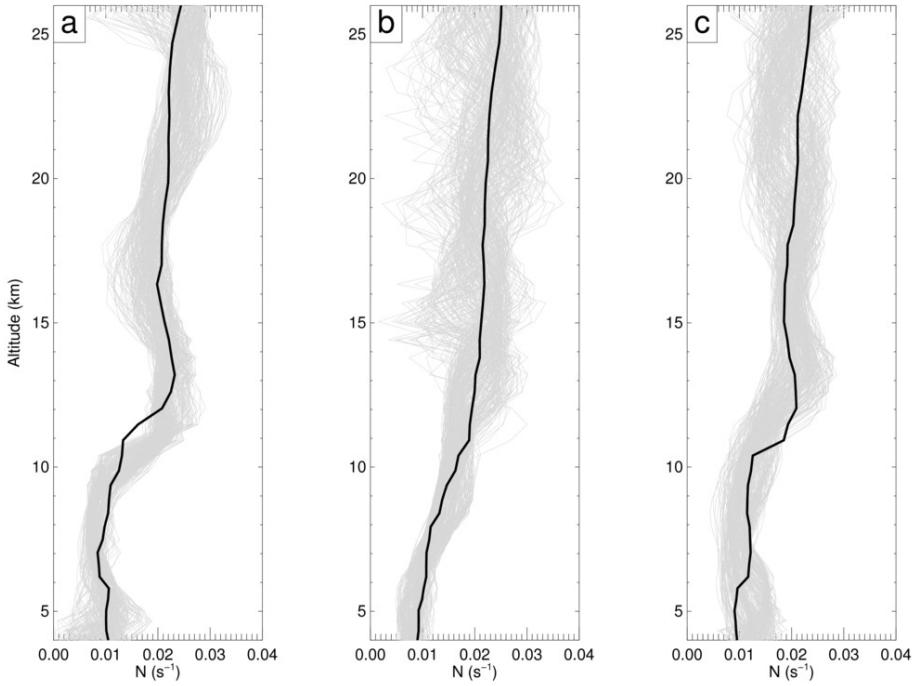

Figure 8. As Fig. 6, but for Brunt–Väisälä frequency N (s^{-1}).

ACPD
14, 18277–18314, 2014

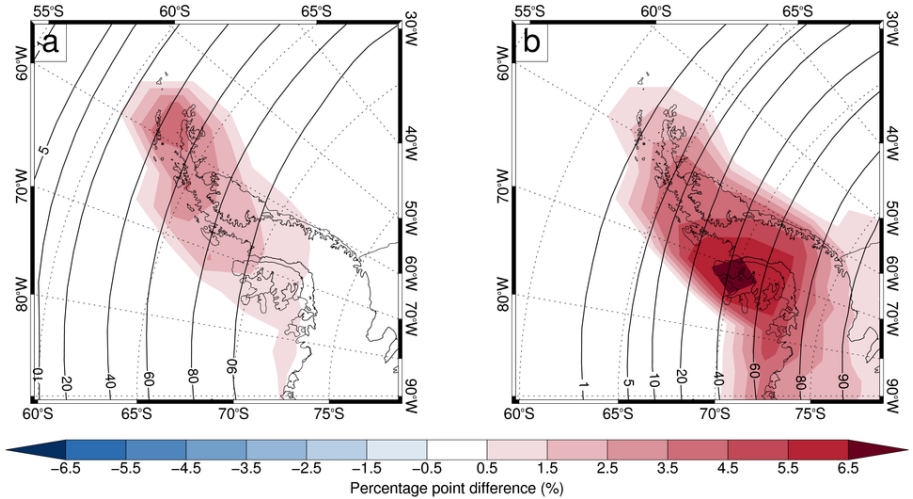

Figure 9. Impact of the mountain wave parameterisation during July at 21 km on the frequency f the 195 K **(a)** and 188 K **(b)** temperature thresholds are exceeded over the Antarctic Peninsula in the perturbation run of the chemistry–climate model. Shown are the 30 year average percentage point difference between the frequency based on the explicitly resolved temperature $T_{\mathrm{CHEM-CLIM}}$ plus the parameterised temperature fluctuations $\Delta T^{-}_{\mathrm{SSO}}$, and the frequency based solely on $T_{\mathrm{CHEM-CLIM}}$, i.e. $f_{T_{\mathrm{CHEM-CLIM}}+\Delta T^{-}_{\mathrm{SSO}}} - f_{T_{\mathrm{CHEM-CLIM}}}$. In the perturbed run, ΔT_{SSO} is represented by the cooling phase $\Delta T^{-}_{\mathrm{SSO}}$ only. The temperature thresholds of 195 and 188 K are assumed to be representative of the formation of type I and II PSCs, respectively. Both differences are computed from 6 hourly fields. The contours indicate the 30 year average frequency $f_{T_{\mathrm{CHEM-CLIM}}}$. Also shown is the coastline of the Antarctic Peninsula.

ACPD
14, 18277–18314, 2014

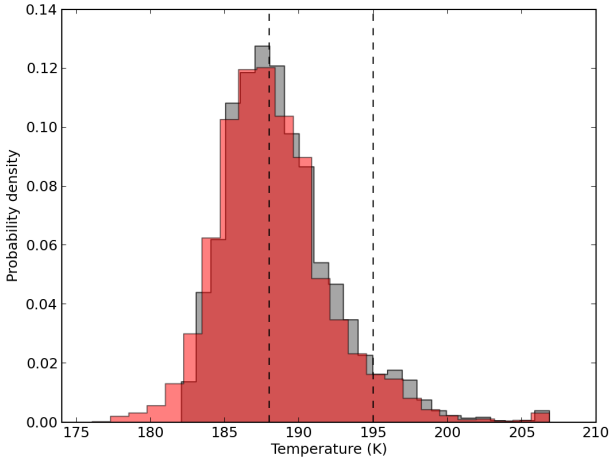

Figure 10. Impact of the mountain wave parameterisation during July at 21 km on the probability distributions of temperature over the Antarctic Peninsula in the perturbed run of the chemistry–climate model. Shown are the 30 year average temperature distributions based on the explicitly resolved temperature $T_{\mathrm{CHEM-CLIM}}$ plus the parameterised temperature fluctuations $\Delta T^{-}_{\mathrm{SSO}}$ (red colouring), and the frequency based solely on $T_{\mathrm{CHEM-CLIM}}$ (gray colouring). Regions where the two distributions overlap is coloured the darker shade of red. Both temperature distributions are for the N48 grid box as used in Figs. 5, 7 and 8. In the perturbed run, ΔT_{SSO} is represented by the cooling phase $\Delta T^{-}_{\mathrm{SSO}}$ only. The temperature thresholds of 195 and 188 K are marked as dashed vertical lines and are assumed to be representative of the formation of type I and II PSCs, respectively. Both temperature distributions are computed from 6 hourly fields.

ACPD
14, 18277–18314, 2014

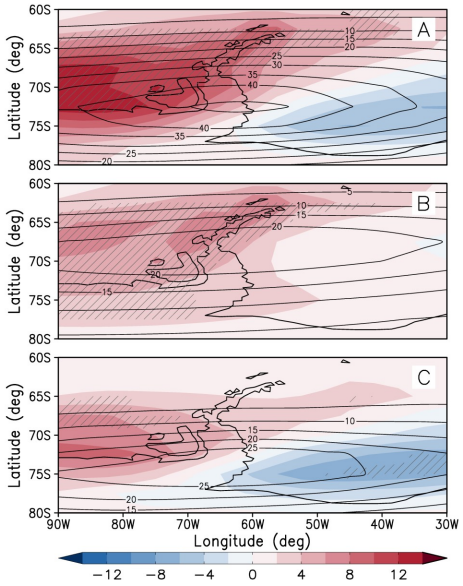

Figure 11. Impact of the mountain wave parameterisation during July at 21 km on PSC surface area density ($\mu m^2\,cm^{-3}$) over the Antarctic Peninsula in the chemistry–climate model. The shading indicates the 30 year average difference in surface area density between the perturbation run and the control run (perturbation run minus the control run) for PSC types I and II **(A)**, type I **(B)**, and type II **(C)**. The contours indicate the 30 year average PSC surface area density from the control run. Hatching denotes significance at the 95 % confidence level using a two-tailed Student's *t* test. Also shown is the coastline of the Antarctic Peninsula.

ACPD
14, 18277–18314, 2014